PCCP

ROYAL SOCIETY OF CHEMISTRY

PAPER

View Article Online
View Journal | View Issue

Cite this: *Phys. Chem. Chem. Phys.*, 2026, **28**, 5715

Generalised level anticrossings explain improved ^{19}F SABRE hyperpolarisation under oscillating magnetic fields

Joni Eronen, * Perttu Hilla, Vladimir V. Zhivonitko, Juha Vaara and Anu M. Kantola *

Received 9th December 2025,
Accepted 2nd February 2026

DOI: 10.1039/d5cp04781a

rsc.li/pccp

Signal amplification by reversible exchange (SABRE) is a parahydrogen-based hyperpolarisation technique that significantly enhances nuclear magnetic resonance signals without the use of expensive hardware. While conventional SABRE relies on a static polarisation transfer field set near the level anticrossing (LAC) condition, recent work has shown that oscillating fields can substantially boost the hyperpolarisation levels. Here, we develop a new theoretical model that generalises the LAC condition to account for the oscillating polarisation transfer fields, thereby explaining the spin dynamics of SABRE under such conditions. We use the generalised LAC condition to optimise the oscillating fields for maximum polarisation transfer to ^{19}F and show that the scalar relaxation of the second kind can be simultaneously suppressed. Large-scale spin dynamics simulations and experiments show that this leads to enhanced ^{19}F hyperpolarisation compared to conventional SABRE, with a 79% improvement observed experimentally. This work demonstrates a generalisable strategy for improving the efficiency of SABRE, advancing its potential for various applications, such as in biomedicine.

1 Introduction

Nuclear magnetic resonance (NMR) spectroscopy and imaging provide chemical, structural, and dynamical information at the molecular level. The NMR signal is usually recorded at a high static magnetic field B_0, where the dominant energy contribution is from the nuclear spin Zeeman interaction. For a spin-1/2 nucleus with a gyromagnetic ratio of γ, the energy splitting between the "spin-up" and "spin-down" states, $|\alpha\rangle$ and $|\beta\rangle$, respectively, is equal to $\hbar\gamma B_0$, where $\hbar$ is the reduced Planck constant. This energy is, at room temperature, much lower than the thermal energy $k_\mathrm{B}T$ given by the Boltzmann constant k_B and temperature T, which, according to the Boltzmann distribution, leads to a small population difference $n_\alpha - n_\beta$ between the $|\alpha\rangle$ and $|\beta\rangle$ states. The resulting spin polarisation

$$P = \frac{n_\alpha - n_\beta}{n_\alpha + n_\beta} \times 100\% = \tanh\left(\frac{\hbar\gamma B_0}{2k_\mathrm{B}T}\right) \times 100\% \qquad (1)$$

is very small near ambient temperatures even in high-field NMR instruments, *e.g.*, $P \approx 3.3 \times 10^{-3}$% for protons at B_0 = 9.4 T and T = 293 K, and even smaller in benchtop spectrometers, where the operating fields are on the order of 1 T, highlighting the sensitivity problem of NMR.

NMR Research Unit, University of Oulu, P.O. Box 3000, Oulu, FI-90014, Finland. E-mail: joni.eronen@oulu.fi, anu.kantola@oulu.fi

The low sensitivity of NMR can be addressed using hyperpolarisation methods,[1] by which the spin polarisation can be increased by several orders of magnitude. This is of particular interest in benchtop NMR, where the thermal spin polarisation is small. Four prominent methods are widely used: dynamic nuclear polarisation (DNP),[2,3] photochemically-induced dynamic nuclear polarisation (photo-CIDNP),[4,5] spin-exchange optical pumping (SEOP),[6] and parahydrogen-induced polarisation (PHIP).[7,8] DNP transfers spin order from unpaired electrons to a target nucleus using microwave irradiation. In photo-CIDNP, light excitation is used to trigger a chemical reaction producing a radical pair, which can be further converted into nuclear spin hyperpolarisation of the molecule of interest. SEOP is used to hyperpolarise noble gases by transferring spin order from optically pumped alkali-metal electrons to the noble-gas nuclei in spin-exchange collisions. Hydrogenative PHIP methods make use of parahydrogen (pH_2)—the singlet nuclear spin isomer of molecular hydrogen—through the hydrogenation of a target molecule and the subsequent conversion of the singlet spin order into observable magnetisation.

Signal amplification by reversible exchange (SABRE)[9–12] is a more recent parahydrogen-based hyperpolarisation technique that addresses the main limitation of PHIP by not requiring unsaturated chemical bonds that can be hydrogenated. In SABRE, pH_2 and the target molecule reversibly bind with an iridium-based complex, enabling conversion of the singlet spin order from pH_2

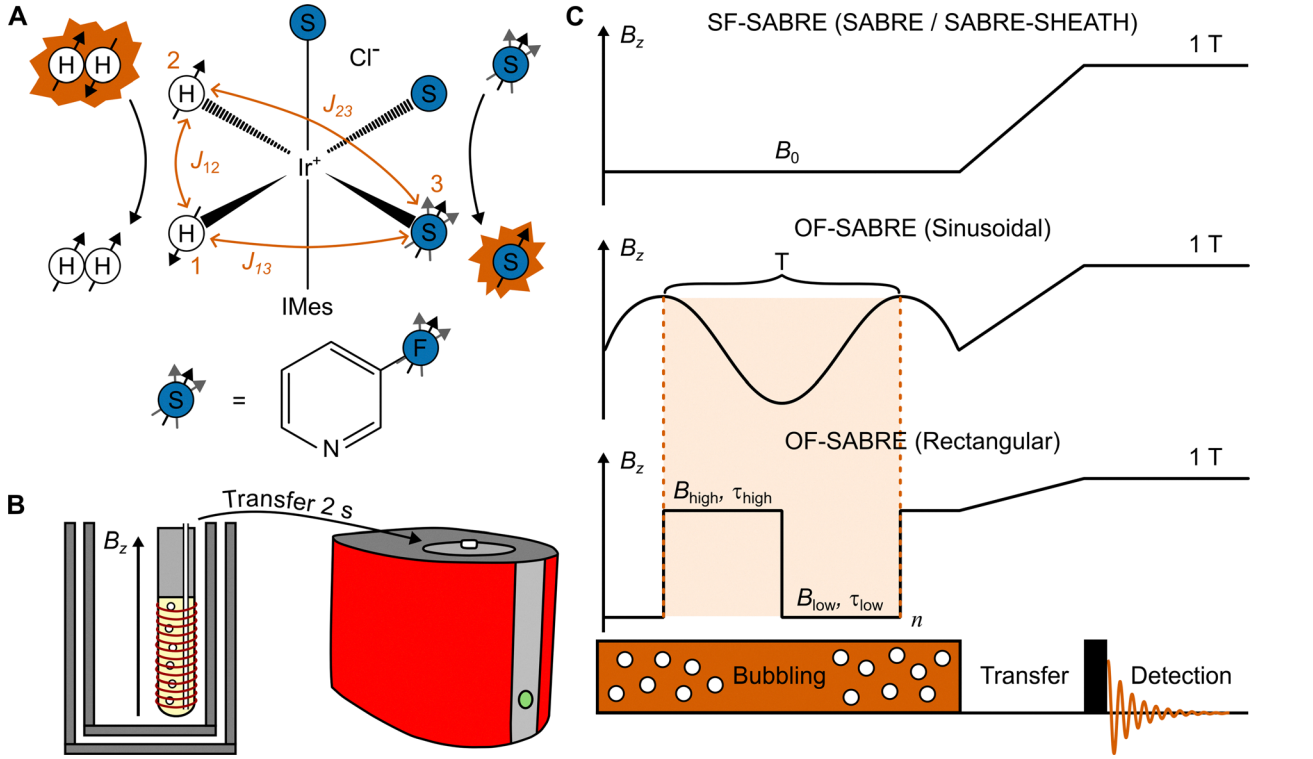

Fig. 1 Overview of the SABRE process. (A) Schematic representation of the chemical kinetics in SABRE. The pH_2 and the target molecule exchange reversibly with the hexacoordinated Ir-complex, which is represented by a three-spin system consisting of two hydride protons (H) and the target nucleus from one of the equatorial ligands (S), with the numbering of the nuclei indicated in the figure. This study examines the ^{19}F nucleus from a 3-fluoropyridine ligand. *J*-couplings between the nuclei, labelled in the picture, enable the conversion of the singlet spin order from pH_2 to observable magnetisation of the target nucleus. (B) Experimental procedure in SABRE. Hyperpolarisation is performed by flushing pH_2 through a sample placed in a 5-mm NMR tube. Subsequently, the gas flow is stopped, and the sample is transferred to the spectrometer for signal acquisition. (C) Variations of SABRE. SF-SABRE utilises a static polarisation transfer field B_0 set at or near the LAC-condition to provide optimum coherent dynamics that transfer the polarisation from the hydrides to the ligand. OF-SABRE employs an oscillating polarisation transfer field that provides more flexibility in tuning the coherent dynamics.

into observable magnetisation of a target nucleus. The SABRE process is shown schematically in Fig. 1A.

In SABRE experiments, the hyperpolarisation is often performed by flushing pH_2 for a few seconds through a sample that is placed in an NMR tube, as demonstrated in Fig. 1B. The experiments typically employ a static polarisation transfer field B_0 adjusted to maximise the coupling between the states involved in the coherent polarisation transfer. This is known as the energy level anticrossing (LAC) condition, which enables efficient SABRE hyperpolarisation.[13,14] For protons, the optimal field strength is typically in the range of a few mT,[15–20] while heteronuclei require fields on the order of μT—a technique that has been named SABRE-SHEATH (SABRE in shield enables alignment transfer to heteronuclei).[21–28] Alternatively, radio-frequency (RF) magnetic fields can be applied to drive the polarisation transfer. Several such RF-based SABRE techniques have been developed to improve the versatility of SABRE or to boost the attainable signal enhancements: LIGHT-SABRE[29] enables coherent polarisation transfer inside the high field of an NMR spectrometer with low-power continuous-wave pulses, SLIC-SABRE[30] induces LAC conditions by using continuous-wave irradiation at low magnetic fields, and QUASR-SABRE[31] is a form of SLIC-SABRE employing interleaved, shaped RF pulses to induce polarisation transfer. While these methods have their own practical applications, they often exhibit lower polarisation transfer compared to the standard static-field approach.

Recent work[32–38] has demonstrated that applying a simple oscillating magnetic field during the polarisation transfer (illustrated in Fig. 1C) allows fine-tuning the coherent spin dynamics to better match the timescale of the ligand exchange. Consequently, the *oscillating-field* SABRE approach has been used to generate increased hyperpolarisation levels compared to the *static-field* SABRE. The static- and oscillating-field SABRE are abbreviated as SF- and OF-SABRE from now on. To date, this technique has been explored on ^{15}N through the hyperpolarisation of ^{15}N-enriched benzonitrile,[32] acetonitrile,[34–36] and metronidazole,[38] yielding also substantial hyperpolarisation in nuclear sites that are several bonds away through spin-relay.[38] In addition, hyperpolarisation of ^{13}C-enriched pyruvate, an important metabolic agent, has been demonstrated.[37]

This work shows, for the first time, the application of oscillating polarisation transfer fields to the SABRE hyperpolarisation of ^{19}F nuclei using 3-fluoropyridine as the target molecule. Hyperpolarisation of ^{19}F is valuable for biomedical applications, as its high natural abundance, large gyromagnetic ratio, and absence of background signals enable highly sensitive detection

of exogenous fluorinated compounds. We establish a robust theoretical framework for understanding the underlying spin physics of the SABRE process under oscillating fields. By applying suitable interaction frame transformations, Floquet theory,[39,40] and average Hamiltonian theory (AHT),[41] we derive an effective time-independent Hamiltonian that drives the OF-SABRE spin dynamics. The analysis reveals a generalised LAC condition that must be fulfilled by the time average of the oscillating field to optimise the polarisation transfer. It is shown that, by tuning the frequency and amplitude of the field, it is possible to adjust the effective coupling between spin states and to suppress scalar relaxation of the second kind (SR2K), a relaxation mechanism that can cause fast relaxation of nuclei that are coupled to a fast-relaxing quadrupolar (nuclear spin ≥ 1) nucleus, especially at low magnetic fields.[42] This theoretical model is validated through comprehensive spin dynamics simulations and SABRE experiments using benchtop NMR, providing a detailed picture of the polarisation transfer process. Notably, an improvement of 79% to the ^{19}F hyperpolarisation levels compared to the SF-SABRE is experimentally obtained, showcasing the potential of the OF-SABRE method, especially for benchtop NMR.

2 Theory

2.1 Static polarisation transfer fields

The theory of the coherent spin order transfer in SABRE under the static polarisation transfer field B_0 is well-established.[10,13,14,43] The nuclear spin Hamiltonian governing the coherent dynamics of a SABRE spin system is given by

$$\hat{H} = \sum_i \omega_i \hat{I}_{zi} + 2\pi \sum_{i<j} J_{ij} \hat{\boldsymbol{I}}_i \cdot \hat{\boldsymbol{I}}_j, \tag{2}$$

where $\omega_i = \omega_{0i}(1 + \delta_i)$ is the resonance frequency of the ith spin, including the Larmor frequency $\omega_{0i} = -\gamma_i B_0$ and the isotropic chemical shift δ_i. The second term represents the scalar J-coupling between spins i and j, with magnitude J_{ij} in Hz. The spin operators $\hat{I}_{zi}$ (z-component for the ith spin) and $\hat{\boldsymbol{I}}_i = (\hat{I}_{xi}, \hat{I}_{yi}, \hat{I}_{zi})$ act on the Hilbert-space ($\mathscr{H}$) state vectors of the spin system.

The spin dynamics of SABRE can be understood qualitatively by analysing the coherent evolution of a simple three-spin model, even though the incoherent processes, namely relaxation and chemical exchange, as well as other spins of the SABRE-complex, must be included in a quantitative model.[44] The simple model includes the two hydride protons originating from the pH_2 and a target nucleus from one of the equatorial ligands. A graphical illustration of the SABRE complex and the three-spin system is presented in Fig. 1A. For theoretical analysis, it is useful to write the Hamiltonian in a basis where the hydride protons are expressed using the singlet–triplet states

$$\begin{aligned} |\mathrm{S}\rangle &= \frac{1}{\sqrt{2}}(|\alpha\beta\rangle - |\beta\alpha\rangle) \\ |\mathrm{T}_+\rangle &= |\alpha\alpha\rangle \\ |\mathrm{T}_0\rangle &= \frac{1}{\sqrt{2}}(|\alpha\beta\rangle + |\beta\alpha\rangle) \\ |\mathrm{T}_-\rangle &= |\beta\beta\rangle \end{aligned} \tag{3}$$

and the target nucleus using the Zeeman states $\{|\alpha\rangle,|\beta\rangle\}$. The eight possible composite states can be grouped by the magnetic quantum number M of the total spin

$$\begin{aligned} M &= +1/2\text{: } \{|\mathrm{S}\alpha\rangle, |\mathrm{T}_+\beta\rangle|\mathrm{T}_0\alpha\rangle\} \\ M &= -1/2\text{: } \{|\mathrm{S}\beta\rangle, |\mathrm{T}_-\alpha\rangle|\mathrm{T}_0\beta\rangle\} \\ M &= +3/2\text{: } \{|\mathrm{T}_+\alpha\rangle\} \\ M &= -3/2\text{: } \{|\mathrm{T}_-\beta\rangle\}. \end{aligned} \tag{4}$$

In this basis, the Hamiltonian in eqn (2) becomes block diagonal with two ($M = \pm 1/2$) 3×3 and two ($M = \pm 3/2$) 1×1 blocks. The 3×3 blocks for $M = +1/2$ and $M = -1/2$ are

$$\begin{array}{c} \\ \langle \mathrm{S}\alpha| \\ \langle \mathrm{T}_+\beta| \\ \langle \mathrm{T}_0\alpha| \end{array} \begin{array}{c} \begin{array}{ccc} |\mathrm{S}\alpha\rangle & |\mathrm{T}_+\beta\rangle & |\mathrm{T}_0\alpha\rangle \end{array} \\ \begin{bmatrix} \frac{-3\pi J_{12} + \omega_3}{2} & \frac{\pi(J_{23} - J_{13})}{\sqrt{2}} & \frac{\pi(J_{13} - J_{23}) + \omega_1 - \omega_2}{2} \\ * & \frac{\pi(J_{12} - J_{13} - J_{23}) + \omega_1 + \omega_2 - \omega_3}{2} & \frac{\pi(J_{13} + J_{23})}{\sqrt{2}} \\ * & * & \frac{\pi J_{12} + \omega_3}{2} \end{bmatrix} \end{array} \tag{5}$$

$$\begin{array}{c} \\ \langle \mathrm{S}\beta| \\ \langle \mathrm{T}_-\alpha| \\ \langle \mathrm{T}_0\beta| \end{array} \begin{array}{c} \begin{array}{ccc} |\mathrm{S}\beta\rangle & |\mathrm{T}_-\alpha\rangle & |\mathrm{T}_0\beta\rangle \end{array} \\ \begin{bmatrix} \frac{-3\pi J_{12} - \omega_3}{2} & \frac{\pi(J_{13} - J_{23})}{\sqrt{2}} & \frac{\pi(J_{23} - J_{13}) + \omega_1 - \omega_2}{2} \\ * & \frac{\pi(J_{12} - J_{13} - J_{23}) - \omega_1 - \omega_2 + \omega_3}{2} & \frac{\pi(J_{13} + J_{23})}{\sqrt{2}} \\ * & * & \frac{\pi J_{12} - \omega_3}{2} \end{bmatrix} \end{array}$$

respectively, whereas the 1 × 1 blocks for $M = \pm 3/2$ do not introduce population transfer between states and can be neglected in the SABRE context. The matrix elements denoted by the asterisks should be filled such that the Hamiltonian is Hermitian.

The initial state in a SABRE experiment is approximately an equal combination of $|S\alpha\rangle$ and $|S\beta\rangle$, as the pH_2 used in the experiments may be assumed to have a purity of 100%, and the polarisation of the target nucleus at thermal equilibrium is very close to zero at the low magnetic-field strengths used during the hyperpolarisation in SABRE. The block diagonal form of the Hamiltonian indicates that either the transition $|S\alpha\rangle \rightarrow |T_+\beta\rangle$ or the transition $|S\beta\rangle \rightarrow |T_-\alpha\rangle$ is responsible for the polarisation transfer, as these involve the two possible initial states and change the state of the target nucleus. The states $|S\alpha\rangle$ and $|T_+\beta\rangle$ (or $|S\beta\rangle$ and $|T_-\alpha\rangle$) become maximally coupled when their corresponding diagonal matrix elements in the Hamiltonian given by eqn (5) become equal. This results in a coherent oscillation between the states, with a frequency determined by the off-diagonal element connecting the two states. Setting the diagonal elements equal and solving for the magnetic field leads to the LAC condition for SF-SABRE

$$B_{\text{SF-LAC}} = \pm\frac{\pi(4J_{12} - J_{13} - J_{23})}{\gamma_1(1+\delta_1) + \gamma_2(1+\delta_2) - 2\gamma_3(1+\delta_3)}. \quad (6)$$

The two solutions indicated by the ± symbol correspond to the $|S\alpha\rangle \rightarrow |T_+\beta\rangle$ and $|S\beta\rangle \rightarrow |T_-\alpha\rangle$ transitions within the $M = +1/2$ and $M = -1/2$ subspaces, respectively.

Let us consider an example three-spin system consisting of the two hydride protons (spins 1 and 2) and the ^{19}F nucleus (spin 3) from the equatorial 3-fluoropyridine ligand of the standard Ir-IMes complex used in SABRE experiments (see Fig. 1A). In the lowest-energy conformation of the complex, the *J*-couplings obtained from a quantum-chemical calculation are $J_{12} = -7.67$ Hz, $J_{13} = -0.05$ Hz, and $J_{23} = 2.08$ Hz.[45] The experimentally determined chemical shifts are $\delta_1 = \delta_2 = -23.1$ ppm and $\delta_3 = -124.2$ ppm. Using these parameters, the LAC condition in eqn (6) for the $|S\beta\rangle \rightarrow |T_-\alpha\rangle$ transition gives $B_0 = 3.26$ μT. Fig. 2A shows results from a spin dynamics simulation of this three-spin model performed at $B_0 = 3.26$ μT. A nearly perfect oscillation between the $|S\beta\rangle$ and $|T_-\alpha\rangle$ states is observed, whereas the populations of the other states remain practically constant, rendering the polarisation transfer to ^{19}F highly efficient. Indeed, our previous work[45] shows that the highest ^{19}F polarisation is obtained at 5 μT, relatively close to the 3.26 μT value predicted by the simple three-spin model.

2.2 Sinusoidal polarisation transfer fields

Below, we extend the analytical SF-SABRE theory to the periodic polarisation transfer fields, building upon the pioneering work by Dagys *et al.*,[33] Eriksson *et al.*,[35] and Li *et al.*[36] We begin by considering a magnetic field that varies sinusoidally in time:

$$B_z(t) = B_0 + B_1\cos(\omega_p t). \quad (7)$$

Here, B_0 is the offset, B_1 is the amplitude, and $\omega_p = 2\pi/T$ is the angular frequency corresponding to the period *T*. General periodic fields are discussed later.

We start from the $M = \pm 1/2$ blocks of the Hamiltonian given in eqn (5) with the time dependence now introduced to the resonance frequencies on account of the fluctuating field: $\omega_i \rightarrow \omega_i(t)$. As we saw earlier, the two transitions responsible for the polarisation transfer are $|S\alpha\rangle \rightarrow |T_+\beta\rangle$ or $|S\beta\rangle \rightarrow |T_-\alpha\rangle$. Therefore, we perform an approximation by considering only the corresponding two-level subspaces, reducing the Hamiltonian in eqn (5) into the 2 × 2 blocks

$$\begin{array}{c} \\ \langle S\alpha| \\ \langle T_+\beta| \end{array} \begin{array}{c} \begin{array}{cc} |S\alpha\rangle & |T_+\beta\rangle \end{array} \\ \begin{bmatrix} \dfrac{-3\pi J_{12} + \omega_3}{2} & \dfrac{\pi(J_{23} - J_{13})}{\sqrt{2}} \\ \dfrac{\pi(J_{23} - J_{13})}{\sqrt{2}} & \dfrac{\pi(J_{12} - J_{13} - J_{23}) + \omega_1 + \omega_2 - \omega_3}{2} \end{bmatrix} \end{array} \quad (8)$$

$$\begin{array}{c} \\ \langle S\beta| \\ \langle T_-\alpha| \end{array} \begin{array}{c} \begin{array}{cc} |S\beta\rangle & |T_-\alpha\rangle \end{array} \\ \begin{bmatrix} \dfrac{-3\pi J_{12} - \omega_3}{2} & \dfrac{\pi(J_{13} - J_{23})}{\sqrt{2}} \\ \dfrac{\pi(J_{13} - J_{23})}{\sqrt{2}} & \dfrac{\pi(J_{12} - J_{13} - J_{23}) - \omega_1 - \omega_2 + \omega_3}{2} \end{bmatrix} \end{array}$$

Any Hermitian 2 × 2 matrix can be decomposed in terms of the Cartesian spin operators $\hat{I}_{x,y,z}$ and the unit operator $\hat{E}$:

$$\begin{aligned} \hat{H} &= a_0\hat{E} + a_x\hat{I}_x + a_y\hat{I}_y + a_z\hat{I}_z \\ &= \begin{bmatrix} a_0 + \frac{1}{2}a_z & \frac{1}{2}(a_x - ia_y) \\ \frac{1}{2}(a_x + ia_y) & a_0 - \frac{1}{2}a_z \end{bmatrix}. \end{aligned} \quad (9)$$

Note that this particular decomposition is done for mathematical convenience; these spin operators do not represent the physical spin of the three-spin system. In our case, coefficients a_i become

$$\begin{aligned} a_0 &= \frac{-\pi(2J_{12} + J_{13} + J_{23}) \pm (\omega_1 + \omega_2)}{4} \\ a_x &= \pm\sqrt{2}\pi(J_{23} - J_{13}) \\ a_y &= 0 \\ a_z &= \frac{-\pi(4J_{12} - J_{13} - J_{23}) \pm (-\omega_1 - \omega_2 + 2\omega_3)}{2}, \end{aligned} \quad (10)$$

where the two solutions indicated by the ± symbol correspond to the $M = \pm 1/2$ blocks, respectively. The identity term

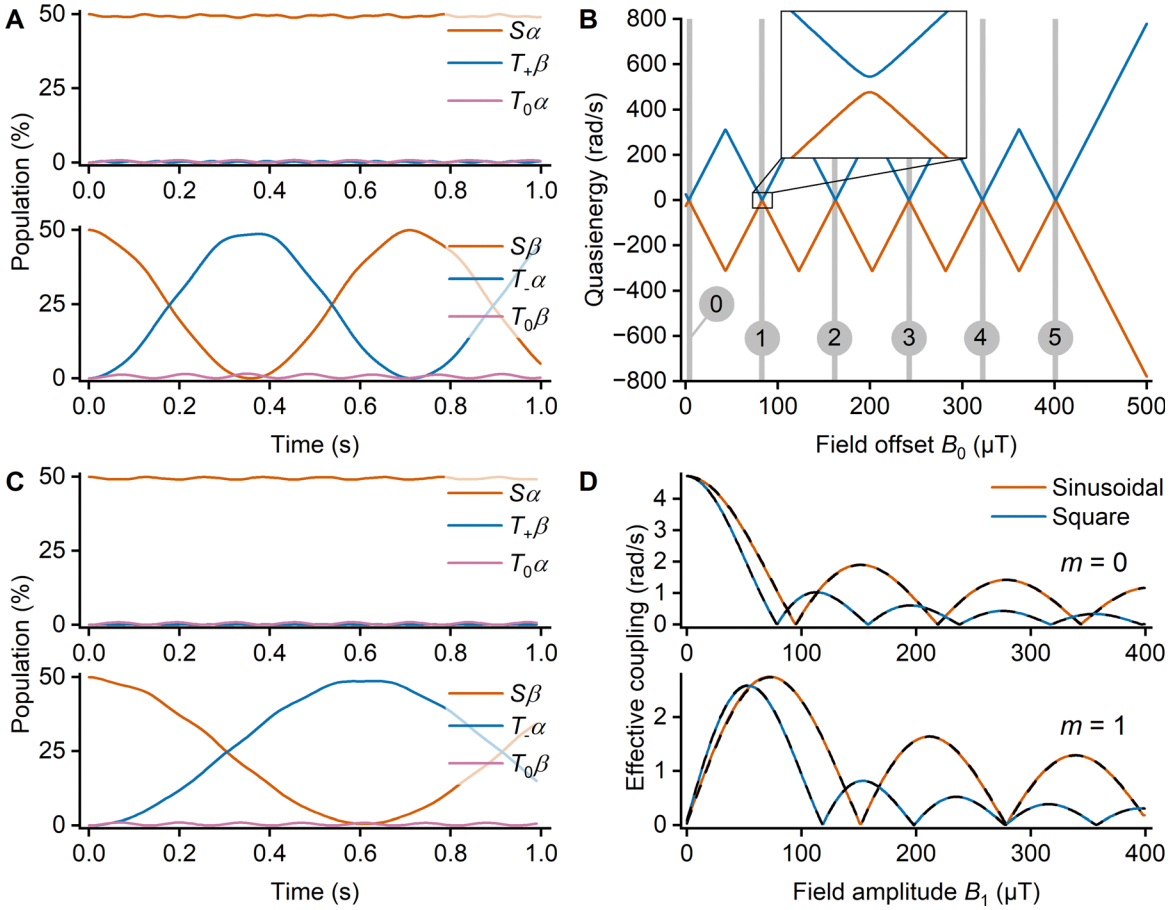

Fig. 2 Spin dynamics simulations of a three-spin SABRE system involving two hydride protons and a ^{19}F nucleus from an equatorial 3-fluoropyridine ligand. (A) Time evolution of the state populations in a SF-SABRE experiment at B_0 = 3.26 μT, starting from equal populations of $|S\alpha\rangle$ and $|S\beta\rangle$. (B) Quasienergies of the SABRE system as a function of field offset B_0 when subjected to a sinusoidal magnetic field $B_0 + B_1\cos[(2\pi/T)t]$ with B_1 = 100 μT and T = 10 ms. The quasienergies are obtained from the numerical diagonalisation of the Floquet matrix that is constructed in a reduced basis including $|k| \leq 5$ Fourier harmonics. The LACs occurring between Floquet modes, separated by integer multiples m of the frequency ω_p, are highlighted, with the m = 1 case magnified in the inset. (C) Time evolution of the state populations in an OF-SABRE experiment using a sinusoidal magnetic field $B_0 + B_1\cos[(2\pi/T)t]$ with B_0 = 43.1 μT, B_1 = 73.2 μT, and T = 10 ms, starting from equal populations of $|S\alpha\rangle$ and $|S\beta\rangle$. (D) Effective coupling strength as a function of the field amplitude B_1 at the m = 0 and m = 1 LACs. The numerically exact values are given for the following effective Hamiltonians: sinusoidal (orange solid) and square-modulated (blue solid) (see Fig. 1C). The analytically calculated values are represented by the black dashes. The period is set to T = 10 ms, for which case m = 0 gives B_0 = 3.26 μT and case m = 1 gives B_0 = 43.1 μT.

$a_0\hat{E}$ can be discarded, as it only shifts the diagonal elements uniformly and, hence, does not affect the transition probabilities. Since the polarisation transfer field follows the time dependence of eqn (7), the component a_z also becomes a sum of the static and sinusoidal components

$$a_z = a_{z0} + a_{z1}\cos(\omega_p t), \tag{11}$$

with the coefficients a_{z0} and a_{z1} given by

$$\begin{aligned} a_{z0} &= -\frac{\pi(4J_{12} - J_{13} - J_{23})}{2} \\ &\pm \frac{B_0[\gamma_1(1+\delta_1) + \gamma_2(1+\delta_2) - 2\gamma_3(1+\delta_3)]}{2} \\ a_{z1} &= \pm \frac{B_1[\gamma_1(1+\delta_1) + \gamma_2(1+\delta_2) - 2\gamma_3(1+\delta_3)]}{2}. \end{aligned} \tag{12}$$

Using this notation, the Hamiltonian becomes

$$\begin{aligned} \hat{H} &= a_x\hat{I}_x + \left[a_{z0} + a_{z1}\cos(\omega_p t)\right]\hat{I}_z \\ &= \frac{1}{2}\begin{bmatrix} a_{z0} + a_{z1}\cos(\omega_p t) & a_x \\ a_x & -a_{z0} - a_{z1}\cos(\omega_p t) \end{bmatrix}. \end{aligned} \tag{13}$$

The ultimate goal is to derive a time-independent effective Hamiltonian using the AHT expansion. The convergence of the expansion can be improved by choosing an interaction frame that removes the large time-dependent part.[41] Thus, we use the time-dependent term $a_{z1}\cos(\omega_p t)\hat{I}_z$ to determine the interaction frame,[36] and the corresponding unitary operator is

$$\begin{aligned} \hat{U}_1 &= \exp\left[ia_{z1}\hat{I}_z\int_0^t \cos(\omega_p t')\mathrm{d}t'\right] \\ &= \exp\left[i\frac{a_{z1}}{\omega_p}\hat{I}_z\sin(\omega_p t)\right]. \end{aligned} \tag{14}$$

The Hamiltonian that drives the spin dynamics in such an interaction frame is given by

$$\begin{aligned}\tilde{H} &= \hat{U}_1\hat{H}\hat{U}_1^\dagger + i\frac{\mathrm{d}\hat{U}_1}{\mathrm{d}t}\hat{U}_1^\dagger = \frac{1}{2}\begin{bmatrix} a_{z0} & a_x e^{i\frac{a_{z1}}{\omega_p}\sin(\omega_p t)} \\ * & -a_{z0}\end{bmatrix} \\ &= \frac{1}{2}\begin{bmatrix} a_{z0} & a_x\sum_{n=-\infty}^{\infty} J_n\left(\frac{a_{z1}}{\omega_p}\right)e^{in\omega_p t} \\ * & -a_{z0}\end{bmatrix},\end{aligned} \tag{15}$$

where we have used the Jacobi–Anger expansion[46] in the last equality, and J_n are the Bessel functions of the first kind.

In the previous work on oscillating polarisation transfer fields,[33,35,36] the effective time-independent Hamiltonian was obtained by applying the AHT to eqn (15). Up to second order, the AHT expansion is given by[41]

$$\tilde{H}_{\mathrm{eff}} = \frac{1}{T}\int_0^T \tilde{H}\mathrm{d}t + \frac{1}{2iT}\int_0^T\int_0^t \left[\tilde{H}(t),\tilde{H}(t')\right]\mathrm{d}t\mathrm{d}t' + \cdots, \tag{16}$$

where T is the period of the Hamiltonian. To the first order, only the term $n = 0$ in the Jacobi-Anger expansion remains non-zero, leading to

$$\begin{aligned}\tilde{H}_{\mathrm{eff}} &\approx \frac{1}{2\pi/\omega_p}\int_0^{2\pi/\omega_p}\tilde{H}\mathrm{d}t \\ &= \frac{1}{2}\begin{bmatrix} a_{z0} & a_x J_0\left(\frac{a_{z1}}{\omega_p}\right) \\ a_x J_0\left(\frac{a_{z1}}{\omega_p}\right) & -a_{z0}\end{bmatrix}.\end{aligned} \tag{17}$$

This is a good approximation when $a_{z0} \approx 0$, *i.e.*, when the average field B_0 is set at or near the LAC condition given by eqn (6), rendering the norm of the Hamiltonian $\tilde{H}$ in eqn (15) to be small. When the norm of the Hamiltonian satisfies $||\tilde{H}||T \ll 1$, the AHT expansion converges rapidly.[41] However, it has been shown that the average field does not have to be near the LAC condition to transfer polarisation efficiently.[34,35] In this case, $a_{z0} \not\approx 0$, and the polarisation transfer cannot be explained by the first-order effective Hamiltonian in eqn (17). Thus, it is evident that the higher-order terms become significant when the average field is not near the LAC condition, requiring a more general theory of OF-SABRE.

Here, we use the Floquet theory[39,40] to explain the polarisation transfer when the offset B_0 is far from the LAC condition. In this formalism, the time-dependent Schrödinger equation is written in the time-independent form

$$\tilde{H}_{\mathrm{F}}|\phi\rangle = \varepsilon_\phi|\phi\rangle, \tag{18}$$

where $\tilde{H}_{\mathrm{F}}$ is the Floquet Hamiltonian, $|\phi\rangle$ the Floquet modes, and ε_ϕ their quasienergies. We use the Fourier expansion of the time-dependent Hamiltonian

$$\tilde{H} = \sum_{n=-\infty}^{\infty}\tilde{H}^{(n)}e^{in\omega_p t} \tag{19}$$

to construct the Floquet Hamiltonian in an infinite-dimensional product Hilbert space $\mathscr{H} \otimes \mathscr{T}$. Here, $\mathscr{T}$ is another Hilbert space that consists of all possible periodic functions with a basis defined by the infinite set of functions $\{e^{ik\omega_p t}\}$, where k is an integer. Thus, the basis set of the product space $\mathscr{H} \otimes \mathscr{T}$ is a set of all the possible Kronecker product pairs $\{|\psi_j\rangle \otimes e^{ik\omega_p t}\}$, where the state vectors $|\psi_j\rangle$ are given in eqn (4). The matrix form of $\tilde{H}_{\mathrm{F}}$ in this basis is given by

$$\tilde{H}_{\mathrm{F}} = \begin{bmatrix} \ddots & \vdots & & & \\ \cdots & \tilde{H}^{(0)} - \omega_p & \tilde{H}^{(-1)} & \tilde{H}^{(-2)} & \\ & \tilde{H}^{(1)} & \tilde{H}^{(0)} & \tilde{H}^{(-1)} & \\ & \tilde{H}^{(2)} & \tilde{H}^{(1)} & \tilde{H}^{(0)} + \omega_p & \cdots \\ & & & \vdots & \ddots \end{bmatrix}, \tag{20}$$

where $\tilde{H}^{(n)}$ are the Fourier components of the time-dependent Hamiltonian. It is evident that the Hamiltonian in eqn (15) can be decomposed into a Fourier series with the components given by

$$\tilde{H}^{(n)} = \frac{1}{2}\begin{bmatrix} \delta_{n0}a_{z0} & a_x J_n\left(\frac{a_{z1}}{\omega_p}\right) \\ a_x J_{-n}\left(\frac{a_{z1}}{\omega_p}\right) & -\delta_{n0}a_{z0}\end{bmatrix}, \tag{21}$$

where δ_{n0} is the Kronecker delta. The Floquet matrix $\tilde{H}_{\mathrm{F}}$ is obtained by substituting the Fourier components $\tilde{H}^{(n)}$ to eqn (20), and is given in eqn (S1) of the SI.

In principle, the quasienergies ε_ϕ can be obtained exactly by constructing and diagonalising the inifinite-dimensional Floquet matrix. In practice, this is not feasible for the SABRE system under study, as the Floquet matrix does not have a block-diagonal decomposition. However, it is trivial to arrive at an approximation numerically. We can reduce the basis set $\{e^{ik\omega_p t}\}$ of the $\mathscr{T}$ space to only include the harmonics $|k| \leq k_{\max}$, which renders the combined space $\mathscr{H} \otimes \mathscr{T}$ finite-dimensional and, thus, enables the construction and diagonalisation of $\tilde{H}_{\mathrm{F}}$ numerically. Using the simple 3-fluoropyridine example system with the basis set reduction $k_{\max} = 5$ and the field amplitude $B_1 = 100$ μT, the Floquet matrix is constructed for the $M = -1/2$ subspace that contains the states $|\mathrm{S}\beta\rangle$ and $|\mathrm{T}_-\alpha\rangle$. The quasienergies, obtained by the numerical diagonalisation of the Floquet matrix, are expressed as a function of the static offset B_0 in Fig. 2B. The appearance of periodic LACs is observed.

Similar to SF-SABRE, the polarisation transfer becomes efficient at the LACs. The LACs emerge when two of the diagonal elements in the Floquet matrix (eqn (S1) in the SI) become equal. This happens when, for some integer m,

$$a_{z0} + m\omega_p = 0, \tag{22}$$

where a_{z0} was given in eqn (12). Inspired by this observation, we define yet another interaction frame with respect to $m\omega_p$ to embed the condition in eqn (22) into the interaction-frame Hamiltonian. In addition, m is chosen such that $|a_{z0} + m\omega_p|$ is

minimised to improve the convergence of AHT in the interaction frame. The transformation operator is defined as

$$\hat{U}_2 = \exp(-i\hat{I}_z m\omega_p t), \tag{23}$$

and the Hamiltonian of eqn (15) in this new interaction frame reads

$$\begin{aligned}\tilde{\hat{H}} &= \hat{U}_2\tilde{H}\hat{U}_2^\dagger + i\frac{\mathrm{d}\hat{U}_2}{\mathrm{d}t}\hat{U}_2^\dagger \\ &= \frac{1}{2}\begin{bmatrix} a_{z0} + m\omega_p & a_x\sum\limits_{n=-\infty}^{\infty} J_n\left(\frac{a_{z1}}{\omega_p}\right)e^{i(n-m)\omega_p t} \\ * & -a_{z0} - m\omega_p \end{bmatrix}.\end{aligned} \tag{24}$$

Finally, we apply the AHT expansion given in eqn (16) up to the first order. This yields the following effective time-independent Hamiltonian:

$$\begin{aligned}\tilde{\hat{H}}_{\mathrm{eff}} &\approx \frac{1}{2\pi/\omega_p}\int_0^{2\pi/\omega_p}\tilde{\hat{H}}\mathrm{d}t \\ &= \frac{1}{2}\begin{bmatrix} a_{z0} + m\omega_p & a_x J_m\left(\frac{a_{z1}}{\omega_p}\right) \\ a_x J_m\left(\frac{a_{z1}}{\omega_p}\right) & -a_{z0} - m\omega_p \end{bmatrix}.\end{aligned} \tag{25}$$

The Hamiltonian in eqn (25) gives critical insights into the polarisation transfer dynamics in OF-SABRE. For efficient polarisation transfer, the diagonal elements must be equal, which, by construction, corresponds to eqn (22). Substituting in the coefficient a_{z0} from eqn (12) and solving for B_0 gives the main theoretical result of the present work: the generalised LAC condition for OF-SABRE, as

$$\begin{aligned}B_{\text{OF-LAC}} &= \pm\frac{\pi(4J_{12} - J_{13} - J_{23}) - 2m\omega_p}{\gamma_1(1+\delta_1) + \gamma_2(1+\delta_2) - 2\gamma_3(1+\delta_3)} \\ &= B_{\text{SF-LAC}} \pm \frac{-2m\omega_p}{\gamma_1(1+\delta_1) + \gamma_2(1+\delta_2) - 2\gamma_3(1+\delta_3)}.\end{aligned} \tag{26}$$

The symbol $\pm$ corresponds to the transitions $|\mathrm{S}\alpha\rangle \rightarrow |\mathrm{T}_+\beta\rangle$ and $|\mathrm{S}\beta\rangle \rightarrow |\mathrm{T}_-\alpha\rangle$, respectively. Comparing to the LAC condition for SF-SABRE, $B_{\text{SF-LAC}}$ given in eqn (6), a new $m\omega_p$-dependent term arises. The new LAC condition explains the appearance of periodic LACs in Fig. 2B and, more importantly, why the polarisation transfer may become efficient in OF-SABRE even when the offset B_0 is far from $B_{\text{SF-LAC}}$. Another important outcome is the introduction of the effective coupling; the off-diagonal term in eqn (25) is now modulated by the mth order Bessel function $J_m(a_{z1}/\omega_p)$, which effectively adjusts the coupling between the spin states. We recall from eqn (12) that the coefficient a_{z1} depends on the field amplitude B_1. Consequently, by adjusting B_1 and the field oscillation frequency ω_p, it is possible to tune the effective coupling such that the resulting coherent polarisation transfer matches the dissociation rate of the ligand in the SABRE complex. However, it must be noted that the effective coupling can only be decreased because $|J_m(a_{z1}/\omega_p)| \leq 1$.

Using the simple 3-fluoropyridine example system discussed earlier, let us calculate the parameters for $m = 1$ when the period of the sinusoidal field is set to $T = 10$ ms. The generalised LAC condition in eqn (26) between states $|\mathrm{S}\beta\rangle$ and $|T_-\alpha\rangle$ gives $B_0 = 43.1$ μT. Suppose we want to maximise the effective coupling in eqn (25). The Bessel function $J_1(a_{z1}/\omega_p)$ reaches its maximum absolute value equal to 0.58 when the argument is equal to ± 1.84, leading to the amplitude $B_1 = \mp 73.2$ μT. The results of a numerical simulation of the three-spin system with these parameters are shown in Fig. 2C. Comparison to the SF-SABRE in Fig. 2A shows that, in OF-SABRE, the interchange between $|\mathrm{S}\beta\rangle$ and $|\mathrm{T}_-\alpha\rangle$ populations takes place at a frequency reduced by a factor of roughly 0.58, as predicted by the decrease of the effective coupling in eqn (25).

Even though the above theory has been derived in the framework of the three-spin system, it applies to a broader range of spin systems including those where multiple heteronuclei of the same type co-exist in the ligand. Further discussion of this issue is presented in the SI.

2.3 General periodic polarisation transfer fields

All periodic functions can be decomposed into Fourier series. This means that also other waveforms of $B_1(t)$ than the sinusoidal one can be treated using the same procedure as above: the first interaction frame is defined by the time-dependent term of the Hamiltonian and the second by $m\omega_p$. Hence, the diagonal elements of the approximate time-independent form of the Hamiltonian, displayed in eqn (25), remain the same. Therefore, the generalised LAC condition given in eqn (26) holds for arbitrary $B_1(t)$ waveforms. The same does not hold in the off-diagonal elements—their analytical treatment becomes challenging, and it is easier to depend on numerical calculations. Further discussion on other waveforms and an analytical expression for square-modulated fields are presented in the SI. The absolute values of the off-diagonal elements that drive the $|\mathrm{S}\beta\rangle \rightarrow |\mathrm{T}_-\alpha\rangle$ transition in the $m = 0$ and $m = 1$ cases, obtained both analytically and numerically for cosine and square waves, are given in Fig. 2D. We see that the effective coupling is very different for the two waveforms. In addition, a remarkable agreement between the presently derived analytical model and the numerical calculations is achieved.

There are two good reasons to opt for other waveforms than sinusoidal. The first reason is the aforementioned different modulation of the off-diagonal elements. Indeed, Li *et al.*[36] have demonstrated that less symmetric waves, such as the saw wave, show better resilience to experimental imperfections due to their more gradual decrease in the coupling strength as a function of the wave amplitude. The second reason comes from the fact that coherent dynamics do not alone determine the maximum achievable polarisation; relaxation plays a major role in the process and can greatly limit the achievable polarisation level. For example, the SR2K mechanism is a major source of relaxation at ultralow fields,[42] the condition at which coherent polarisation transfer to heteronuclei is optimal. This is the case in the present 3-fluoropyridine system, as the ^{19}F is scalar-coupled to the quadrupolar ^{14}N nucleus.

3 Results and discussion

3.1 Periodic LACs on large spin systems

The above discussion focused on the simple three-spin model without taking into account relaxation and chemical exchange. To verify the existence of the periodic LACs in a more realistic SABRE setting involving 3-fluoropyridine, we performed experiments and large-scale numerical spin dynamics simulations. The simulations incorporated a chemically exchanging system consisting of the SABRE complex (8 spins), free ligand (6 spins), and parahydrogen (2 spins), as well as full Redfield-theory[47–49] relaxation. Details of the experiments and simulations are available in the SI. Various rectangular-shaped polarisation transfer fields (see Fig. 1C), characterised by B_{high}, B_{low}, τ_{high}, and τ_{low}, were used.

Fig. 3A shows the experimental and simulated ^{19}F polarisation levels as a function of B_{high}, with the other parameters fixed to B_{low} = 3 μT (close to the LAC condition for SF-SABRE) and $\tau_{high} = \tau_{low}$ = 5 ms or $\tau_{high} = \tau_{low}$ = 10 ms. Maximum ^{19}F polarisation level of 0.55% was obtained at B_{high} = 8 μT. This result is as expected, since the average field of roughly 5 μT is near the LAC condition for SF-SABRE and this particular field value has been experimentally shown to generate the highest polarisation levels.[45] When B_{high} is increased further, more local maxima (and minima) are observed both experimentally and computationally, in agreement with the obtained generalised LAC condition in eqn (26). With $\tau_{high} = \tau_{low}$ = 5 ms, we find a local (negative) maximum at B_{high} = 68 μT with a ^{19}F polarisation of −0.26%. This corresponds to the generalised LAC condition with $m = -1$ between the $|S\alpha\rangle$ and $|T_+\beta\rangle$ states. In turn, a local maximum with a ^{19}F polarisation of 0.28% is observed at B_{high} = 88 μT, corresponding to the generalised LAC condition between $|S\beta\rangle$ and $|T_-\alpha\rangle$ with $m = 1$. With the longer field duration of $\tau_{high} = \tau_{low}$ = 10 ms, we observe local maxima and minima of the polarisation level twice as frequently, showcasing the LACs with $m = 0$, $m = \pm 1$ and $m = \pm 2$ (see eqn (26)) within the studied magnetic field range. Experiments on ^{1}H under the same field conditions did not produce substantial hyperpolarisation levels, as shown in Fig. S3 of the SI.

The present spin dynamics simulations, which qualitatively reproduce the experimental magnetic-field dependence, are seen to overestimate the achieved polarisation levels. This

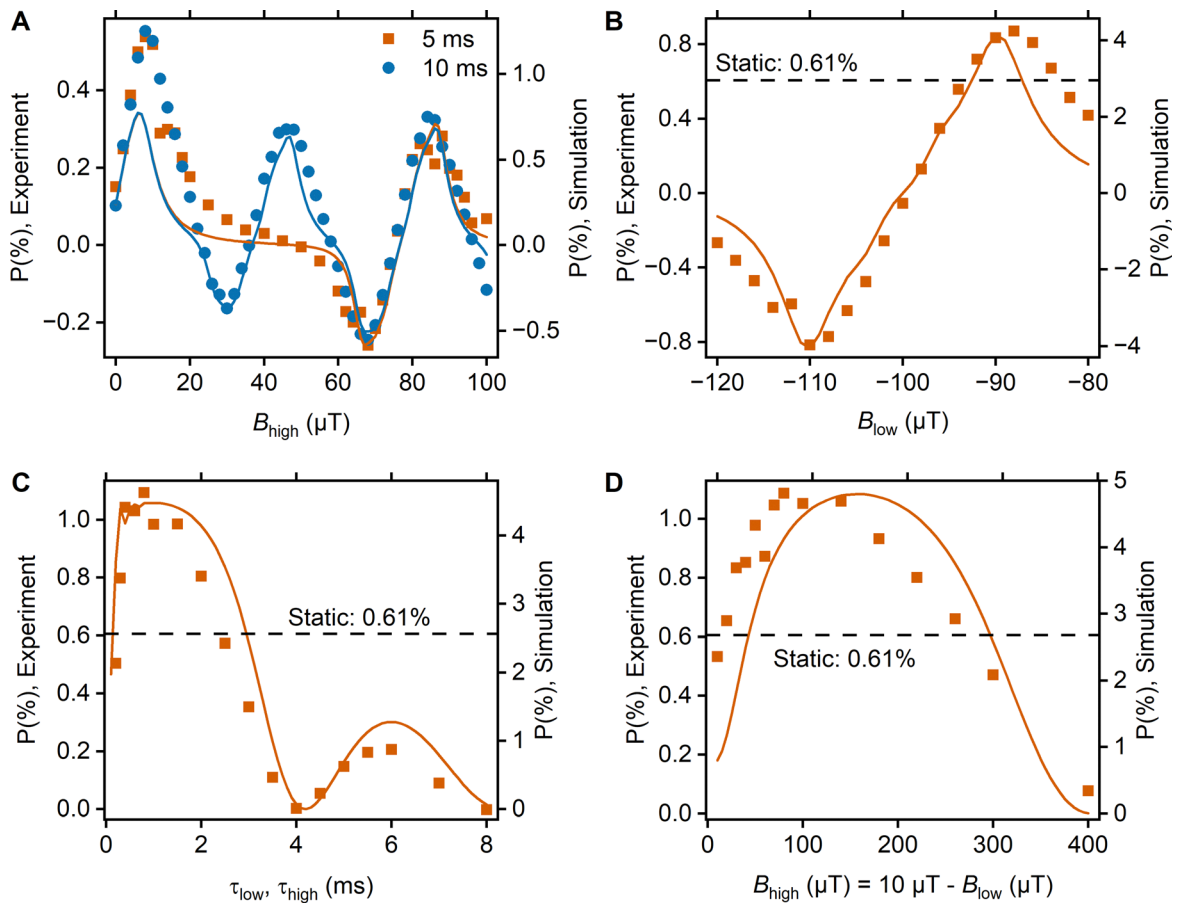

Fig. 3 Experimental and simulated ^{19}F spin polarisation in OF-SABRE. Square-modulated polarisation transfer field, characterised by B_{high}, B_{low}, and $\tau_{high} = \tau_{low}$ (see Fig. 1C), is used. Results from experiments (left vertical axis) are shown as symbols and from simulations (right vertical axis) as solid lines. The maximum polarisation obtained in SF-SABRE is denoted by a dashed horizontal line. (A) Polarisation as a function of B_{high}. The other parameters are B_{low} = 3 μT and $\tau_{high} = \tau_{low}$ = 5 ms (orange squares) or $\tau_{high} = \tau_{low}$ = 10 ms (blue circles). (B) Polarisation as a function of B_{low}. The other parameters are B_{high} = 100 μT and $\tau_{high} = \tau_{low}$= 2 ms. (C) Polarisation as a function of $\tau_{high} = \tau_{low}$, with B_{high} = 100 μT and B_{low} = − 90 μT. (D) Polarisation as a function of the field amplitude defined by B_{high} and B_{low}, with $\tau_{high} = \tau_{low}$ = 1 ms.

trend is present in all the simulation results. However, the results are remarkably accurate considering that the simulations use the isotropic rotational diffusion of a rigid molecule as the dynamical model within the Redfield theory. Other major approximations responsible for the discrepancies between the simulations and experiments are including only 8 spins in the SABRE complex model, and not incorporating all the reaction intermediates[50] in the exchange process.

With the 3-fluoropyridine ligand at room temperature, we find lower polarisation levels at the $|m| \geq 1$ LACs with OF-SABRE as compared to the SF-SABRE, which resulted in polarisation of 0.61% at the optimum field of 5 μT. This result differs from the data obtained previously on ^{15}N-acetonitrile, where higher ^{15}N polarisation levels were obtained using OF-SABRE.[35,36] The most important difference between the ^{15}N and ^{19}F systems is the order-of-magnitude difference in the *J*-coupling between the hydride protons and the target nucleus. In the ^{15}N system, the *J*-coupling is J_{NH} = 25.41 Hz,[35] whereas in the 3-fluoropyridine system, the quantum-chemically obtained *J*-coupling only amounts to J_{FH} = 2.08 Hz. This is important, because the use of oscillating polarisation transfer fields that satisfy the $|m| \geq 1$ LACs reduces the effective coupling, as demonstrated in Fig. 2D. In the case of the very large *J*-coupling of the ^{15}N-system, it is useful to reduce the effective coupling, such that the coherent dynamics are optimal with respect to the ligand dissociation rate, which results in better polarisation levels. In contrast, the *J*-coupling in the present ^{19}F system is already small, and reducing it further leads to smaller polarisation levels.

3.2 Improving polarisation levels using oscillating fields

The above theoretical analysis suggests that rectangular polarisation-transfer field profiles may be used to improve the ^{19}F polarisation levels by incorporating the two concepts: first, the offset $B_0 = (B_{high} + B_{low})/2$ is tuned to match the $m = 0$ LAC given by eqn (26) to maximise the effective coupling. Second, a sufficiently large amplitude $B_1 = (B_{high} - B_{low})/2$ is applied such that the total magnetic field stays away from the regime where the SR2K leads to increased relaxation rates. Consequently, we next choose to apply B_{high} = 100 μT and systematically adjust B_{low}. With $\tau_{high} = \tau_{low}$ = 2 ms, this yields better polarisation levels than SF-SABRE, as seen in Fig. 3B. Again, a maximum and a minimum (negative maximum) are observed, corresponding to the ± LACs with m = 0 given by eqn (26). The maximum negative ^{19}F polarisation of −0.81% is found at B_{low} = −110 μT and the maximum positive polarisation of 0.87% at B_{low} = −88 μT. The result is interesting, as neither B_{high} or B_{low} is close to the optimum static field of 5 μT. In fact, the use of either B_{high} or B_{low} alone as the polarisation transfer field produces nearly zero polarisation transfer to ^{19}F.[45] Again, the time average of the field at these optimum conditions is approximately ±5 μT, which coincides with the optimum static field for ^{19}F. Hyperpolarisation of ^{1}H remains inefficient under such field conditions, as shown in Fig. S4 of the SI.

The efficiency of ^{19}F SABRE can be further improved by optimising the field durations $\tau_{high} = \tau_{low}$ at the polarisation transfer fields of B_{high} = 100 μT and B_{low} = −90 μT, as shown in Fig. 3C. The optimum field duration is approximately 0.8 ms, with the maximum polarisation level of 1.09%. This improves the maximum achievable ^{19}F hyperpolarisation by 79% over SF-SABRE. Shorter field durations are less effective both in experiments and simulations. This observation is expected, because the oscillating-field component effectively vanishes in the limit $\omega_p \to \infty$, at which the system experiences only the static average field. On the other hand, increasing the field duration past the optimum also decreases the polarisation transfer, *e.g.*, giving near zero polarisation at 4 ms. This outcome aligns with the theoretical model; the effective coupling for the square wave (eqn (S10) in the SI), modulated by the frequency ω_p, vanishes at $\tau_{high} = \tau_{low}$ = 4 ms, which means that no polarisation can be transferred. Increasing the field duration further again shows a local maximum at 6 ms, corresponding to a local maximum in the effective coupling.

The final parameter that can be optimised is the field amplitude. Fig. 3D shows results where the amplitude is increased by simultaneously varying B_{high} and B_{low}, while the time average of the magnetic field is maintained at 5 μT. With the amplitude of approximately 100 μT, the maximum polarisation of 1.09% is achieved. When the amplitude is smaller, a smaller polarisation is observed, which can be understood from the field dependence of relaxation. At very small magnetic fields, ^{19}F relaxation is enhanced by the presence of the quadrupolar ^{14}N nucleus *via* the SR2K mechanism.[42] On the other hand, increasing the magnetic field past the optimum leads to a lower level of hyperpolarisation. This effect is essentially the same as when modifying the field duration—the effective coupling is reduced, which results in a lower polarisation level.

All the above experiments used a square-modulated polarisation transfer field. However, significant ^{19}F hyperpolarisation can be obtained even with an asymmetric rectangular wave, as long as the time average of the field remains near the optimum static field of 5 μT. To showcase this, experiments and simulations were performed with field durations of τ_{high} = 2 ms and τ_{low} = 1 ms while fixing B_{high} = 50 μT and varying B_{low} from −150 μT to −50 μT. The results of these experiments and the corresponding simulations are shown in Fig. S5 of the SI. The highest enhancements are observed with the B_{low} values of −116 μT or −84 μT, resulting in polarisation levels of −0.92% and 0.98%, respectively. Again, these values coincide with the time average of the field being roughly equal to ±5 μT.

3.3 Relaxation under oscillating fields

Relaxation times at varying field conditions were studied to elucidate the underlying reasons for the efficacy of OF-SABRE. Three different fields were used: one oscillating between B_{high} = 100 μT and B_{low} = − 90 μT with the field durations of $\tau_{high} = \tau_{low}$ = 2 ms, a static 5 μT field, and a static 100 μT field. The resulting experimental relaxation times for ^{19}F are shown in Fig. 4A. It is found that the longitudinal relaxation time increases from T_1 = 5.4 s to T_1 = 10.1 s when changing from the static magnetic field of 5 μT to the oscillating field. This increase in T_1 is the key reason for the enhanced polarisation levels achieved with OF-SABRE compared to SF-SABRE; the use

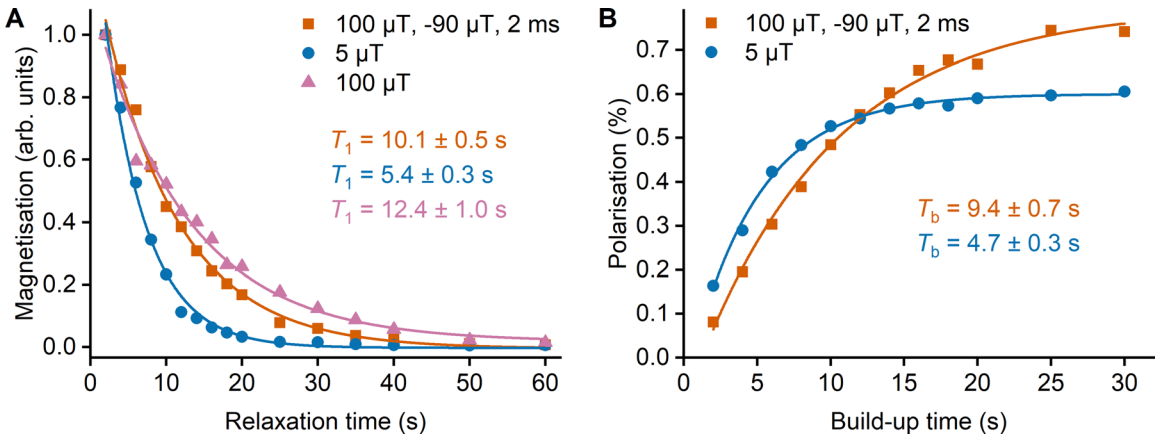

Fig. 4 Experimental relaxation and build-up dynamics of ^{19}F spin polarisation at selected magnetic fields. Square-modulated field with B_{high} = 100 μT, B_{low} = −90 μT, and τ_{high} = τ_{low} = 2 ms (orange squares); static 5 μT field (blue circles); and static 100 μT field (pink triangles). The solid lines show an exponential fit, from which the indicated (A) T_1 relaxation times and (B) polarisation build-up times T_b are extracted.

of a field that oscillates between B_{high} = 100 μT and B_{low} = −90 μT maximises the coherent dynamics similarly to a static 5 μT field, while simultaneously diminishing the relaxation rate. The reference measurement at the static 100 μT field shows a slightly longer relaxation time of T_1 = 12.4 s, as compared to the oscillating field. The difference could be explained by the coherent dynamics, which are very different in the two field conditions, but a detailed explanation would require further investigation. In addition, experimental imperfections in the oscillating field might induce faster relaxation.

The experimentally observed differences in the relaxation times were reproduced qualitatively by the spin dynamics simulations, resulting in T_1 = 9.4 s with the oscillating field, T_1 = 1.5 s at 5 μT, and T_1 = 27.7 s at 100 μT, as shown in Fig. S6 of the SI. The lack of quantitative agreement between the simulated and experimental relaxation times is again likely to be caused by using the simple isotropic rotational diffusion as the dynamical model, as well as not including all the spins of the SABRE complex.

The T_1 relaxation time of ^{1}H was also studied under the three field conditions. Both the experimental results in Fig. S7 as well as the simulation results in Fig. S8 of the SI show the shortest relaxation times at the static 5 μT field, followed by the values obtained using the oscillating field and the static 100 μT field, in this order, with the T_1 times comparable to those of ^{19}F.

3.4 Polarisation build-up under oscillating fields

Build-up times of ^{19}F polarisation were studied to further understand the efficiency of OF-SABRE. The build-up curve was experimentally and computationally determined using a square-modulated field with B_{high} = 100 μT, B_{low} = −90 μT, and τ_{high} = τ_{low} = 2 ms, as well as with the static field of 5 μT. The experimental results are shown in Fig. 4B. The build-up time T_b under the oscillating field is 9.4 s whereas a faster build-up of T_b = 4.7 s is recorded at the static 5 μT field. Both values are in agreement with the relaxation times shown in Fig. 4A. This is expected, as relaxation determines the upper limit for the build-up time. The simulated build-up times shown in Fig. S9 of the SI display a comparable result. In conclusion, the suppression of SR2K by using an oscillating transfer field leads to increased relaxation times, allowing a longer effective build-up time, which improves the ^{19}F polarisation level.

4 Conclusions

In this work, using a combination of suitable interaction frame transformations, Floquet theory, and average Hamiltonian theory, we have derived a new theoretical model for oscillating polarisation transfer fields in SABRE. The theory unveils that efficient polarisation transfer under oscillating fields boils down to two important principles: First, the generalised LAC condition for some integer multiple m of the frequency ω_p, given by eqn (26), must be fulfilled by the static offset field B_0, causing the states involved in the polarisation transfer to become maximally coupled. Second, the field amplitude B_1 and the frequency ω_p must be chosen such that the effective coupling is optimised with respect to the dissociation rate of the ligand in the SABRE complex. For example, in the sinusoidal oscillating field case, the effective coupling is modulated by the m:th order Bessel function $J_m(a_{z1}/\omega_p)$ where the parameter a_{z1} depends on B_1.

We have validated the theoretically predicted effects *via* large-scale spin dynamics simulations and SABRE experiments by demonstrating the hyperpolarisation of ^{19}F on a 3-fluoropyridine system using benchtop NMR. Suggested by the theory, we have shown that choosing a rectangular field pattern with the static offset of 5 μT and an amplitude of approximately 100 μT, with short field duration of 0.8 ms, enables optimal coherent dynamics while suppressing the fast ^{19}F relaxation induced by scalar relaxation of the second kind. Such conditions lead into an improvement of 79% in the ^{19}F polarisation over the static-field SABRE. A similar approach is directly applicable to the hyperpolarisation of any heteronucleus in spin systems that suffer from fast relaxation at ultralow fields.

We expect that the established principles enable a more systematic optimisation of future SABRE experiments, bridging

the gap between laboratory studies and real-world applications through the improvement of signal enhancement.

Author contributions

J. E. conceptualisation, formal analysis, investigation, methodology, software, visualisation, writing – original draft. P. H. methodology, software, writing – review & editing. V. V. Z. funding acquisition, resources, writing – review & editing. J. V. conceptualisation, funding acquisition, resources, supervision, writing – review & editing. A. M. K. conceptualisation, funding acquisition, supervision, writing – review & editing.

Conflicts of interest

There are no conflicts to declare.

Data availability

All data for this article, including Jupyter notebooks supporting the theoretical discussion, SpinSolve spectrometer files, data processing scripts, and spin dynamics simulation results with the necessary Spinguin scripts are available at Fairdata Etsin.[51] The codes are also accessible *via* the GitHub repository of the project.[52]

Supplementary information (SI): experimental and spin dynamics modelling details, additional theoretical discussion, and additional experimental results. See DOI: https://doi.org/10.1039/d5cp04781a.

Acknowledgements

We acknowledge funding from the Research Council of Finland grants 351357 (A. M. K.), 361326 (J. V.) and 362959 (V. V. Z.), as well as from the Kvantum Institute, University of Oulu.

References

1 J. Eills, D. Budker, S. Cavagnero, E. Y. Chekmenev, S. J. Elliott, S. Jannin, A. Lesage, J. Matysik, T. Meersmann, T. Prisner, J. A. Reimer, H. Yang and I. V. Koptyug, *Chem. Rev.*, 2023, **123**, 1417–1551.
2 A. W. Overhauser, *Phys. Rev.*, 1953, **92**, 411–415.
3 T. R. Carver and C. P. Slichter, *Phys. Rev.*, 1953, **92**, 212–213.
4 J. Bargon, H. Fischer and U. Johnsen, *Z. Naturforsch. A*, 1967, **22**, 1551–1555.
5 H. R. Ward and R. G. Lawler, *J. Am. Chem. Soc.*, 1967, **89**, 5518–5519.
6 T. G. Walker and W. Happer, *Rev. Mod. Phys.*, 1997, **69**, 629–642.
7 C. R. Bowers and D. P. Weitekamp, *Phys. Rev. Lett.*, 1986, **57**, 2645–2648.
8 C. R. Bowers and D. P. Weitekamp, *J. Am. Chem. Soc.*, 1987, **109**, 5541–5542.
9 R. W. Adams, J. A. Aguilar, K. D. Atkinson, M. J. Cowley, P. I. P. Elliott, S. B. Duckett, G. G. R. Green, I. G. Khazal, J. Lopez-Serrano and D. C. Williamson, *Science*, 2009, **323**, 1708–1711.
10 R. W. Adams, S. B. Duckett, R. A. Green, D. C. Williamson and G. G. R. Green, *J. Chem. Phys.*, 2009, **131**, 194505.
11 K. D. Atkinson, M. J. Cowley, P. I. P. Elliott, S. B. Duckett, G. G. R. Green, J. Lopez-Serrano and A. C. Whitwood, *J. Am. Chem. Soc.*, 2009, **131**, 13362–13368.
12 K. D. Atkinson, M. J. Cowley, S. B. Duckett, P. I. P. Elliott, G. G. R. Green, J. Lopez-Serrano, I. G. Khazal and A. C. Whitwood, *Inorg. Chem.*, 2009, **48**, 663–670.
13 A. N. Pravdivtsev, A. V. Yurkovskaya, H.-M. Vieth, K. L. Ivanov and R. Kaptein, *Chem. Phys. Chem.*, 2013, **14**, 3327–3331.
14 K. L. Ivanov, A. N. Pravdivtsev, A. V. Yurkovskaya, H.-M. Vieth and R. Kaptein, *Prog. Nucl. Magn. Reson. Spectrosc.*, 2014, **81**, 1–36.
15 M. J. Cowley, R. W. Adams, K. D. Atkinson, M. C. R. Cockett, S. B. Duckett, G. G. R. Green, J. A. B. Lohman, R. Kerssebaum, D. Kilgour and R. E. Mewis, *J. Am. Chem. Soc.*, 2011, **133**, 6134–6137.
16 E. B. Dücker, L. T. Kuhn, K. Münnemann and C. Griesinger, *J. Magn. Reson.*, 2012, **214**, 159–165.
17 H. Zeng, J. Xu, J. Gillen, M. T. McMahon, D. Artemov, J.-M. Tyburn, J. A. Lohman, R. E. Mewis, K. D. Atkinson, G. G. Green, S. B. Duckett and P. C. van Zijl, *J. Magn. Reson.*, 2013, **237**, 73–78.
18 L. S. Lloyd, A. Asghar, M. J. Burns, A. Charlton, S. Coombes, M. J. Cowley, G. J. Dear, S. B. Duckett, G. R. Genov, G. G. R. Green, L. A. R. Highton, A. J. J. Hooper, M. Khan, I. G. Khazal, R. J. Lewis, R. E. Mewis, A. D. Roberts and A. J. Ruddlesden, *Catal. Sci. Technol.*, 2014, **4**, 3544–3554.
19 R. E. Mewis, K. D. Atkinson, M. J. Cowley, S. B. Duckett, G. G. R. Green, R. A. Green, L. A. R. Highton, D. Kilgour, L. S. Lloyd, J. A. B. Lohman and D. C. Williamson, *Magn. Reson. Chem.*, 2014, **52**, 358–369.
20 A. N. Pravdivtsev, K. L. Ivanov, A. V. Yurkovskaya, P. A. Petrov, H.-H. Limbach, R. Kaptein and H.-M. Vieth, *J. Magn. Reson.*, 2015, **261**, 73–82.
21 T. Theis, M. L. Truong, A. M. Coffey, R. V. Shchepin, K. W. Waddell, F. Shi, B. M. Goodson, W. S. Warren and E. Y. Chekmenev, *J. Am. Chem. Soc.*, 2015, **137**, 1404–1407.
22 M. L. Truong, T. Theis, A. M. Coffey, R. V. Shchepin, K. W. Waddell, F. Shi, B. M. Goodson, W. S. Warren and E. Y. Chekmenev, *J. Phys. Chem. C*, 2015, **119**, 8786–8797.
23 V. V. Zhivonitko, I. V. Skovpin and I. V. Koptyug, *Chem. Commun.*, 2015, **51**, 2506–2509.
24 D. A. Barskiy, R. V. Shchepin, A. M. Coffey, T. Theis, W. S. Warren, B. M. Goodson and E. Y. Chekmenev, *J. Am. Chem. Soc.*, 2016, **138**, 8080–8083.
25 R. V. Shchepin, D. A. Barskiy, A. M. Coffey, T. Theis, F. Shi, W. S. Warren, B. M. Goodson and E. Y. Chekmenev, *ACS Sens.*, 2016, **1**, 640–644.
26 R. V. Shchepin, B. M. Goodson, T. Theis, W. S. Warren and E. Y. Chekmenev, *Chem. Phys. Chem.*, 2017, **18**, 1961–1965.
27 D. A. Barskiy, R. V. Shchepin, C. P. N. Tanner, J. F. P. Colell, B. M. Goodson, T. Theis, W. S. Warren and E. Y. Chekmenev, *Chem. Phys. Chem.*, 2017, **18**, 1493–1498.

28 A. M. Olaru, T. B. R. Robertson, J. S. Lewis, A. Antony, W. Iali, R. E. Mewis and S. B. Duckett, *ChemistryOpen*, 2018, **7**, 97–105.
29 T. Theis, M. Truong, A. M. Coffey, E. Y. Chekmenev and W. S. Warren, *J. Magn. Reson.*, 2014, **248**, 23–26.
30 S. Knecht, A. S. Kiryutin, A. V. Yurkovskaya and K. L. Ivanov, *Mol. Phys.*, 2019, **117**, 2762–2771.
31 N. M. Ariyasingha, J. R. Lindale, S. L. Eriksson, G. P. Clark, T. Theis, R. V. Shchepin, N. V. Chukanov, K. V. Kovtunov, I. V. Koptyug, W. S. Warren and E. Y. Chekmenev, *J. Phys. Chem. Lett.*, 2019, **10**, 4229–4236.
32 J. R. Lindale, S. L. Eriksson, C. P. N. Tanner, Z. Zhou, J. F. P. Colell, G. Zhang, J. Bae, E. Y. Chekmenev, T. Theis and W. S. Warren, *Nat. Commun.*, 2019, **10**, 395.
33 L. Dagys, C. Bengs and M. H. Levitt, *J. Chem. Phys.*, 2021, **155**, 154201.
34 A. N. Pravdivtsev, N. Kempf, M. Plaumann, J. Bernarding, K. Scheffler, J.-B. Hövener and K. Buckenmaier, *Chem. Phys. Chem.*, 2021, **22**, 2381–2386.
35 S. L. Eriksson, J. R. Lindale, X. Li and W. S. Warren, *Sci. Adv.*, 2022, **8**, eabl3708.
36 X. Li, J. R. Lindale, S. L. Eriksson and W. S. Warren, *Phys. Chem. Chem. Phys.*, 2022, **24**, 16462–16470.
37 S. Nantogma, S. L. Eriksson, I. Adelabu, I. Mandzhieva, A. Browning, P. TomHon, W. S. Warren, T. Theis, B. M. Goodson and E. Y. Chekmenev, *J. Phys. Chem. A*, 2022, **126**, 9114–9123.
38 S. Nantogma, S. L. Eriksson, T. Theis, W. S. Warren, B. M. Goodson and E. Y. Chekmenev, *J. Magn. Reson. Open*, 2025, **24**, 100208.
39 J. H. Shirley, *Phys. Rev.*, 1965, **138**, B979–B987.
40 H. Sambe, *Phys. Rev. A*, 1973, **7**, 2203–2213.
41 A. Brinkmann, *Concepts Magn. Reson. A*, 2016, **45A**, e21414.
42 J. R. Birchall, M. S. H. Kabir, O. G. Salnikov, N. V. Chukanov, A. Svyatova, K. V. Kovtunov, I. V. Koptyug, J. G. Gelovani, B. M. Goodson, W. Pham and E. Y. Chekmenev, *Chem. Commun.*, 2020, **56**, 9098–9101.
43 D. A. Barskiy, S. Knecht, A. V. Yurkovskaya and K. L. Ivanov, *Prog. Nucl. Magn. Reson. Spectrosc.*, 2019, **114–115**, 33–70.
44 J. R. Lindale, S. L. Eriksson, C. P. N. Tanner and W. S. Warren, *Sci. Adv.*, 2020, **6**, eabb6874.
45 J. Eronen, S. K.-M. Svensson, N. Hossain, V. V. Zhivonitko, J. Vaara and A. M. Kantola, *Phys. Chem. Chem. Phys.*, 2025, **27**, 13305–13314.
46 G. B. Arfken, H. J. Weber and F. E. Harris, *Mathematical Methods for Physicists*, Academic Press, Boston, 7th edn, 2013, pp. 643–713.
47 A. G. Redfield, *IBM J. Res. Dev.*, 1957, **1**, 19–31.
48 M. Goldman, *J. Magn. Reson.*, 2001, **149**, 160–187.
49 P. Hilla and J. Vaara, *J. Magn. Reson.*, 2025, **372**, 107828.
50 K. Lin, P. TomHon, S. Lehmkuhl, R. Laasner, T. Theis and V. Blum, *Chem. Phys. Chem.*, 2021, **22**, 1947–1957.
51 J. Eronen, *Data repository of the project*, https://doi.org/10.23729/fd-83ba92b6-9142-3884-a667-7f5791ab0564.
52 J. Eronen, *GitHub repository of the project*, https://github.com/nmroulu/OF-SABRE-Project, Accessed: 2025-11-12.